

000 054
 001 055
 002 056
 003 057
 004 058
 005 059
 006 060
 007 061
 008 062
 009 063
 010 064
 011 065
 012 066
 013 067
 014 068
 015 069
 016 070
 017 071
 018 072
 019 073
 020 074
 021 075
 022 076
 023 077
 024 078
 025 079
 026 080
 027 081
 028 082
 029 083
 030 084
 031 085
 032 086
 033 087
 034 088
 035 089
 036 090
 037 091
 038 092
 039 093
 040 094
 041 095
 042 096
 043 097
 044 098
 045 099
 046 100
 047 101
 048 102
 049 103
 050 104
 051 105
 052 106
 053 107

Supplementary File to “Multi-channel Weighted Nuclear Norm Minimization for Real Color Image Denoising”

Anonymous ICCV submission

Paper ID 572

In this supplementary file, we provide:

1. The proof of the Theorem 1 in the main paper.
2. More denoising results on the 24 high quality images from the Kodak PhotoCD dataset.
3. More visual comparisons of denoised images by different methods on the real noisy images of the dataset [1].
4. More visual comparisons of denoised images by different methods on the real noisy images of the dataset [2].

1. Proof of Theorem 1.

Theorem 1. Assume that the weights in w are in a non-descending order, the sequence $\{\mathbf{X}_k\}$, $\{\mathbf{Z}_k\}$, and $\{\mathbf{A}_k\}$ generated in Algorithm 1 satisfy:

$$(a) \lim_{k \rightarrow \infty} \|\mathbf{X}_{k+1} - \mathbf{Z}_{k+1}\|_F = 0; \quad (b) \lim_{k \rightarrow \infty} \|\mathbf{X}_{k+1} - \mathbf{X}_k\|_F = 0; \quad (c) \lim_{k \rightarrow \infty} \|\mathbf{Z}_{k+1} - \mathbf{Z}_k\|_F = 0. \quad (1)$$

Proof. 1. Firstly, we prove that the sequence $\{\mathbf{A}_k\}$ generated by Algorithm 1 is upper bounded. Let $\mathbf{X}_{k+1} + \rho_k^{-1} \mathbf{A}_k = \mathbf{U}_k \Sigma_k \mathbf{V}_k^\top$ be its singular value decomposition (SVD) [3] in the $(k+1)$ -th iteration. According to Corollary 1 of [4], we can have the SVD of \mathbf{Z}_{k+1} as $\mathbf{Z}_{k+1} = \mathbf{U}_k \hat{\Sigma}_k \mathbf{V}_k^\top = \mathbf{U}_k \mathcal{S}_{\frac{w}{\rho_k}}(\Sigma_k) \mathbf{V}_k^\top$. Then we have

$$\|\mathbf{A}_{k+1}\|_F = \|\mathbf{A}_k + \rho_k(\mathbf{X}_{k+1} - \mathbf{Z}_{k+1})\|_F = \rho_k \|\rho_k^{-1} \mathbf{A}_k + \mathbf{X}_{k+1} - \mathbf{Z}_{k+1}\|_F \quad (2)$$

$$= \rho_k \|\mathbf{U}_k \Sigma_k \mathbf{V}_k^\top - \mathbf{U}_k \mathcal{S}_{\frac{w}{\rho_k}}(\Sigma_k) \mathbf{V}_k^\top\|_F = \rho_k \|\Sigma_k - \mathcal{S}_{\frac{w}{\rho_k}}(\Sigma_k)\|_F \quad (3)$$

$$= \rho_k \sqrt{\sum_i (\Sigma_k^{ii} - \mathcal{S}_{\frac{w}{\rho_k}}(\Sigma_k^{ii}))^2} \leq \rho_k \sqrt{\sum_i \left(\frac{w_i}{\rho_k}\right)^2} = \sqrt{\sum_i w_i^2}. \quad (4)$$

The inequality in the second last step can be proved as follows: given the diagonal matrix Σ_k , we define Σ_k^{ii} as the i -th element of Σ_k^{ii} . If $\Sigma_k^{ii} \geq \frac{w_i}{\rho_k}$, we have $\mathcal{S}_{\frac{w}{\rho_k}}(\Sigma_k^{ii}) = \Sigma_k^{ii} - \frac{w_i}{\rho_k} \geq 0$. If $\Sigma_k^{ii} < \frac{w_i}{\rho_k}$, we have $\mathcal{S}_{\frac{w}{\rho_k}}(\Sigma_k^{ii}) = 0 < \Sigma_k^{ii} + \frac{w_i}{\rho_k}$. After all, we have $|\Sigma_k^{ii} - \mathcal{S}_{\frac{w}{\rho_k}}(\Sigma_k^{ii})| \leq \frac{w_i}{\rho_k}$ and hence the inequality holds true. Hence, the sequence $\{\mathbf{A}_k\}$ is upper bounded.

2. Secondly, we prove that the sequence of Lagrangian function $\{\mathcal{L}(\mathbf{X}_{k+1}, \mathbf{Z}_{k+1}, \mathbf{A}_k, \rho_k)\}$ is also upper bounded. Since the global optimal solution of \mathbf{X} and \mathbf{Z} in corresponding subproblems, we always have $\mathcal{L}(\mathbf{X}_{k+1}, \mathbf{Z}_{k+1}, \mathbf{A}_k, \rho_k) \leq \mathcal{L}(\mathbf{X}_k, \mathbf{Z}_k, \mathbf{A}_k, \rho_k)$. Based on the updating rule that $\mathbf{A}_{k+1} = \mathbf{A}_k + \rho_k(\mathbf{X}_{k+1} - \mathbf{Z}_{k+1})$, we have $\mathcal{L}(\mathbf{X}_{k+1}, \mathbf{Z}_{k+1}, \mathbf{A}_{k+1}, \rho_{k+1}) = \mathcal{L}(\mathbf{X}_{k+1}, \mathbf{Z}_{k+1}, \mathbf{A}_k, \rho_k) + \langle \mathbf{A}_{k+1} - \mathbf{A}_k, \mathbf{X}_{k+1} - \mathbf{Z}_{k+1} \rangle + \frac{\rho_{k+1} - \rho_k}{2} \|\mathbf{X}_{k+1} - \mathbf{Z}_{k+1}\|_F^2 = \mathcal{L}(\mathbf{X}_{k+1}, \mathbf{Z}_{k+1}, \mathbf{A}_k, \rho_k) + \frac{\rho_{k+1} + \rho_k}{2\rho_k^2} \|\mathbf{A}_{k+1} - \mathbf{A}_k\|_F^2$. Since the sequence $\{\|\mathbf{A}_k\|_F\}$ is upper bounded, the sequence $\{\|\mathbf{A}_{k+1} - \mathbf{A}_k\|_F\}$ is also upper bounded. Denote by a the upper bound of $\{\|\mathbf{A}_{k+1} - \mathbf{A}_k\|_F\}$, we have $\mathcal{L}(\mathbf{X}_{k+1}, \mathbf{Z}_{k+1}, \mathbf{A}_{k+1}, \rho_{k+1}) \leq \mathcal{L}(\mathbf{X}_1, \mathbf{Z}_1, \mathbf{A}_0, \rho_0) + a \sum_{k=0}^{\infty} \frac{\rho_{k+1} + \rho_k}{2\rho_k^2} = \mathcal{L}(\mathbf{X}_1, \mathbf{Z}_1, \mathbf{A}_0, \rho_0) + a \sum_{k=0}^{\infty} \frac{\mu+1}{2\mu^k \rho_0} \leq \mathcal{L}(\mathbf{X}_1, \mathbf{Z}_1, \mathbf{A}_0, \rho_0) + \frac{a}{\rho_0} \sum_{k=0}^{\infty} \frac{1}{\mu^{k-1}}$. The last inequality holds since $\mu+1 < 2\mu$. Since $\sum_{k=0}^{\infty} \frac{1}{\mu^{k-1}} < \infty$, the sequence of Lagrangian function $\{\mathcal{L}(\mathbf{X}_{k+1}, \mathbf{Z}_{k+1}, \mathbf{A}_{k+1}, \rho_{k+1})\}$ is upper bound.

3. Thirdly, we prove that the sequences of $\{\mathbf{X}_k\}$ and $\{\mathbf{Z}_k\}$ are upper bounded. Since $\|\mathbf{W}(\mathbf{Y} - \mathbf{X})\|_F^2 + \|\mathbf{Z}\|_{w,*} = \mathcal{L}(\mathbf{X}_k, \mathbf{Z}_k, \mathbf{A}_{k-1}, \rho_{k-1}) - \langle \mathbf{A}_k, \mathbf{X}_k - \mathbf{Z}_k \rangle - \frac{\rho_k}{2} \|\mathbf{X}_k - \mathbf{Z}_k\|_F^2 = \mathcal{L}(\mathbf{X}_k, \mathbf{Z}_k, \mathbf{A}_{k-1}, \rho_{k-1}) + \frac{1}{2\rho_k} (\|\mathbf{A}_{k-1}\|_F^2 - \|\mathbf{A}_k\|_F^2)$. Thus $\{\mathbf{W}(\mathbf{Y} - \mathbf{X}_k)\}$ and $\{\mathbf{Z}_k\}$ are upper bounded, and hence the sequence $\{\mathbf{X}_k\}$ is bounded by the Cauchy-Schwarz inequality

Table 1. PSNR(dB) results of different denoising methods on 24 natural images.

Image#	$\sigma_r = 5, \sigma_g = 30, \sigma_b = 15$								
	CBM3D	MLP	TNRD	NI	NC	WNNM-1	WNNM-2	WNNM-3	MC-WNNM
1	27.25	28.06	28.62	25.00	29.55	28.16	27.95	28.15	
2	29.70	31.30	32.70	27.80	29.69	32.54	31.60	31.73	
3	30.34	31.98	34.07	28.02	31.93	33.91	33.68	33.52	
4	29.47	31.10	32.56	27.70	32.56	32.68	31.85	31.90	
5	27.31	28.59	29.35	26.14	30.00	28.83	29.00	28.91	
6	28.20	29.10	29.90	26.15	28.81	29.55	29.46	29.62	
7	29.73	31.60	33.46	27.22	31.63	33.09	33.29	32.86	
8	27.47	28.16	28.91	25.34	30.16	29.15	29.24	29.03	
9	30.07	31.63	33.55	27.86	31.54	33.19	33.20	32.95	
10	29.96	31.37	33.20	27.74	33.44	32.98	33.02	32.74	
11	28.73	29.85	30.87	26.98	30.16	30.45	30.14	30.21	
12	30.20	31.50	33.31	27.97	31.69	33.22	32.71	32.65	
13	26.18	26.69	26.98	25.14	27.97	26.49	26.42	26.62	
14	27.86	29.07	29.87	26.67	29.21	29.36	29.14	29.30	
15	29.91	31.58	33.13	28.04	31.17	33.22	32.34	32.36	
16	29.29	30.35	31.54	27.46	32.18	31.34	31.05	31.21	
17	29.50	31.09	32.52	27.81	32.80	32.09	32.00	31.85	
18	27.72	28.74	29.36	26.57	28.63	28.88	28.76	28.89	
19	28.98	30.18	31.35	27.25	29.79	31.34	30.77	30.95	
20	30.63	31.78	33.27	27.89	29.52	33.00	32.55	32.58	
21	28.50	29.58	30.54	26.86	31.71	30.02	30.03	30.03	
22	28.61	29.78	30.82	27.19	30.50	30.47	29.82	30.10	
23	30.60	32.66	35.06	28.17	32.82	34.72	34.37	33.94	
24	27.97	28.81	29.61	26.01	30.75	29.47	29.35	29.39	
Average	28.92	30.19	31.44	27.04	30.76	31.17	30.91	30.89	32.70

and triangle inequality. We can obtain that $\lim_{k \rightarrow \infty} \|\mathbf{X}_{k+1} - \mathbf{Z}_{k+1}\|_F = \lim_{k \rightarrow \infty} \rho_k^{-1} \|\mathbf{A}_{k+1} - \mathbf{A}_k\|_F = 0$ and the equation (a) is proved.

4. Then we can prove that $\lim_{k \rightarrow \infty} \|\mathbf{X}_{k+1} - \mathbf{X}_k\|_F = \lim_{k \rightarrow \infty} \|(\mathbf{W}^\top \mathbf{W} + \frac{\rho_k}{2} \mathbf{I})^{-1} (\mathbf{W}^\top \mathbf{W} \mathbf{Y} - \mathbf{W}^\top \mathbf{W} \mathbf{Z}_k - \frac{1}{2} \mathbf{A}_k) - \rho_k^{-1} (\mathbf{A}_k - \mathbf{A}_{k-1})\|_F \leq \lim_{k \rightarrow \infty} \|(\mathbf{W}^\top \mathbf{W} + \frac{\rho_k}{2} \mathbf{I})^{-1} (\mathbf{W}^\top \mathbf{W} \mathbf{Y} - \mathbf{W}^\top \mathbf{W} \mathbf{Z}_k - \frac{1}{2} \mathbf{A}_k)\|_F + \rho_k^{-1} \|\mathbf{A}_k - \mathbf{A}_{k-1}\|_F = 0$ and hence (b) is proved.

5. Finally, (c) can be proved by checking that $\lim_{k \rightarrow \infty} \|\mathbf{Z}_{k+1} - \mathbf{Z}_k\|_F = \lim_{k \rightarrow \infty} \|\mathbf{X}_k + \rho_k^{-1} \mathbf{A}_{k-1} - \mathbf{Z}_k + \mathbf{X}_{k+1} - \mathbf{X}_k + \rho_k^{-1} \mathbf{A}_{k-1} + \rho_k^{-1} \mathbf{A}_k - \rho_k^{-1} \mathbf{A}_{k+1}\|_F \leq \lim_{k \rightarrow \infty} \|\Sigma_{k-1} - \mathcal{S}_{w/\rho_{k-1}}(\Sigma_{k-1})\|_F + \|\mathbf{X}_{k+1} - \mathbf{X}_k\|_F + \rho_k^{-1} \|\mathbf{A}_{k-1} + \mathbf{A}_{k+1} - \mathbf{A}_k\|_F = 0$, where $\mathbf{U}_{k-1} \Sigma_{k-1} \mathbf{V}_{k-1}^\top$ is the SVD of the matrix $\mathbf{X}_k + \rho_{k-1} \mathbf{A}_{k-1}$. \square

2. More denoising results on the 24 high quality images from the Kodak PhotoCD dataset

In the main paper, we have given the PSNR results of the competing methods on the 24 high quality images from the Kodak PhotoCD dataset when the standard deviations of the additive white Gaussian noise (AWGN) are $\sigma_r = 40, \sigma_g = 20, \sigma_b = 30$ for R, G, B channels, respectively. Here we provide more denoising results on this dataset. In Tables ??-??, we give more PSNR results on these images when the noise standard deviations are $\sigma_r = 5, \sigma_g = 30, \sigma_b = 15$ in Table 1 and $\sigma_r = 30, \sigma_g = 10, \sigma_b = 50$ in Table 2, respectively. In Figures 4-??, we give the visual comparisons of the denoised images by different methods.

216

217

218

219

220

221

222

223

224

225

226

227

228

229

230

231

232

233

234

235

236

237

238

239

240

241

242

243

244

245

246

247

248

249

250

251

252

253

254

255

256

257

258

259

260

261

262

263

264

265

266

267

268

269

270

271

272

273

274

275

276

277

278

279

280

281

282

283

284

285

286

287

288

289

290

291

292

293

294

295

296

297

298

299

300

301

302

303

304

305

306

307

308

309

310

311

312

313

314

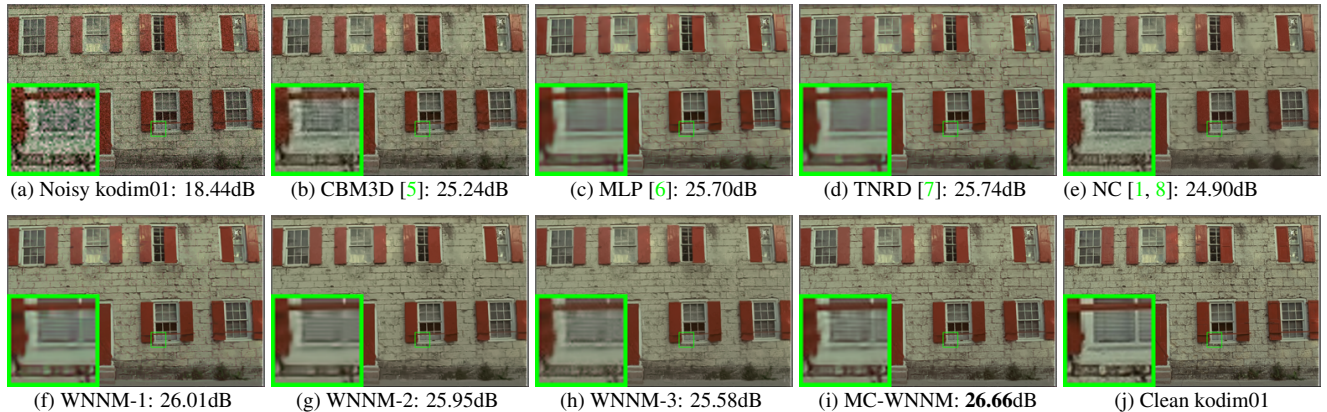
315

316

317

Table 2. PSNR(dB) results of different denoising methods on 24 natural images.

Image#	$\sigma_r = 30, \sigma_g = 10, \sigma_b = 50$								
	CBM3D	MLP	TNRD	NI	NC	WNNM-1	WNNM-2	WNNM-3	MC-WNNM
1	23.38	26.49	26.50	24.82	23.59	26.40	25.60		
2	25.19	30.94	30.90	26.82	27.79	30.89	29.75		
3	25.39	32.03	32.09	27.52	27.41	32.20	31.17		
4	24.96	30.55	30.47	27.34	27.00	30.74	29.71		
5	23.29	26.65	26.73	25.72	26.67	26.74	25.98		
6	24.09	27.76	27.70	26.10	26.12	27.85	26.96		
7	24.89	30.70	30.72	27.17	28.07	30.91	29.94		
8	23.30	26.12	26.27	25.59	26.11	26.87	26.33		
9	25.20	31.35	31.31	27.74	28.33	31.30	30.45		
10	25.13	31.01	31.05	27.60	28.53	31.12	30.17		
11	24.54	28.79	28.82	26.72	24.40	28.73	27.79		
12	25.43	31.60	31.60	27.82	29.01	31.59	30.62		
13	22.50	24.71	24.73	24.96	23.36	24.70	23.85		
14	23.91	27.69	27.72	26.26	23.08	27.62	26.81		
15	25.45	31.09	31.05	27.36	28.49	31.29	30.21		
16	24.89	29.79	29.73	27.35	27.10	29.84	28.85		
17	25.12	30.26	30.24	27.15	27.54	30.11	29.35		
18	23.83	27.26	27.26	26.05	26.15	27.32	26.18		
19	24.63	29.40	29.39	27.06	27.41	29.78	28.87		
20	26.43	31.16	31.27	26.43	26.92	31.25	30.43		
21	24.24	28.26	28.27	26.66	27.18	28.22	27.45		
22	24.51	29.03	29.06	26.83	27.64	29.02	27.81		
23	25.55	32.87	32.75	27.60	23.75	32.58	31.46		
24	23.85	27.06	27.13	25.86	27.05	27.50	26.63		
Average		24.57	29.27	29.28	26.69	26.61	29.36	28.43	29.90

Figure 1. Denoised images of different methods on the image "kodim01" degraded by AWGN with different standard deviations of $\sigma_r = 40, \sigma_g = 20, \sigma_b = 30$ on R, G, B channels, respectively. The images are better to be zoomed in on screen.

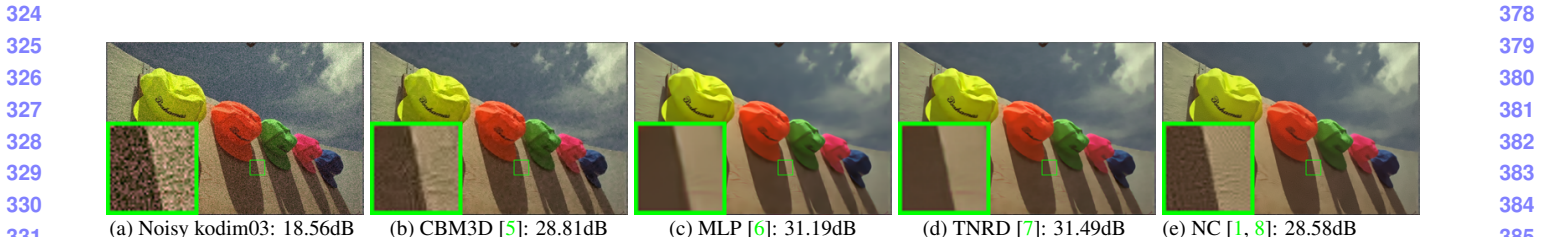


Figure 2. Denoised images of different methods on the image “kodim03” degraded by AWGN with different standard deviations of $\sigma_r = 40$, $\sigma_g = 20$, $\sigma_b = 30$ on R, G, B channels, respectively. The images are better to be zoomed in on screen.

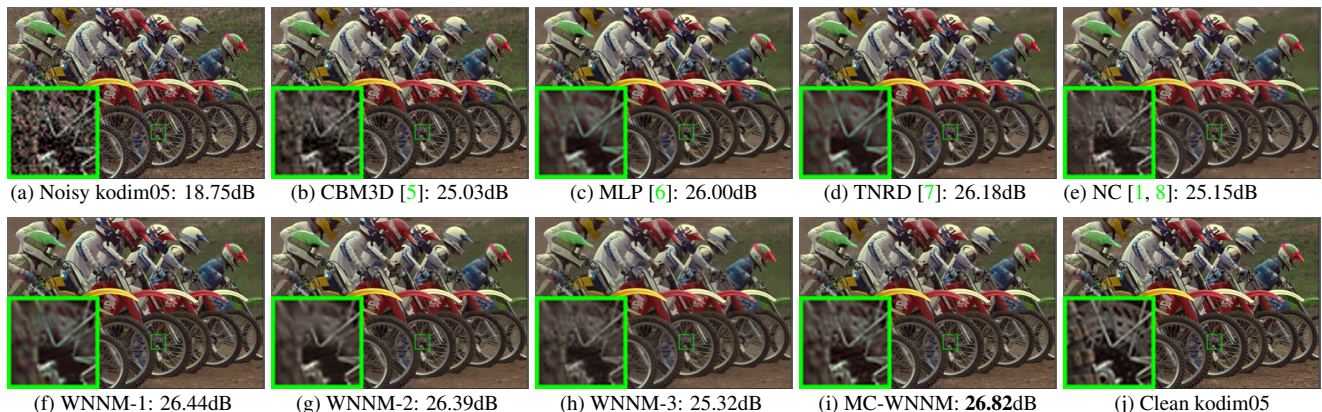


Figure 3. Denoised images of different methods on the image “kodim05” degraded by AWGN with different standard deviations of $\sigma_r = 40$, $\sigma_g = 20$, $\sigma_b = 30$ on R, G, B channels, respectively. The images are better to be zoomed in on screen.

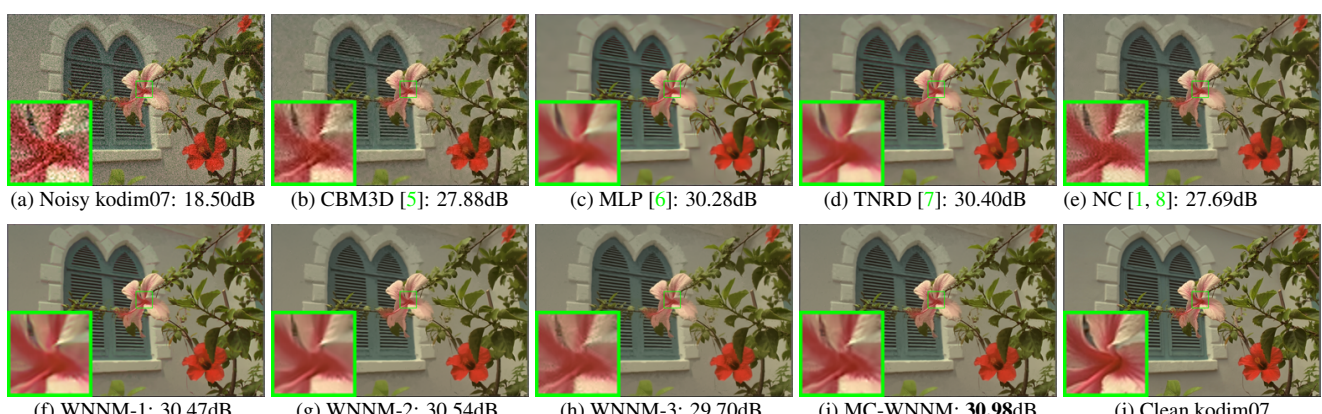


Figure 4. Denoised images of different methods on the image “kodim07” degraded by AWGN with different standard deviations of $\sigma_r = 40$, $\sigma_g = 20$, $\sigma_b = 30$ on R, G, B channels, respectively. The images are better to be zoomed in on screen.

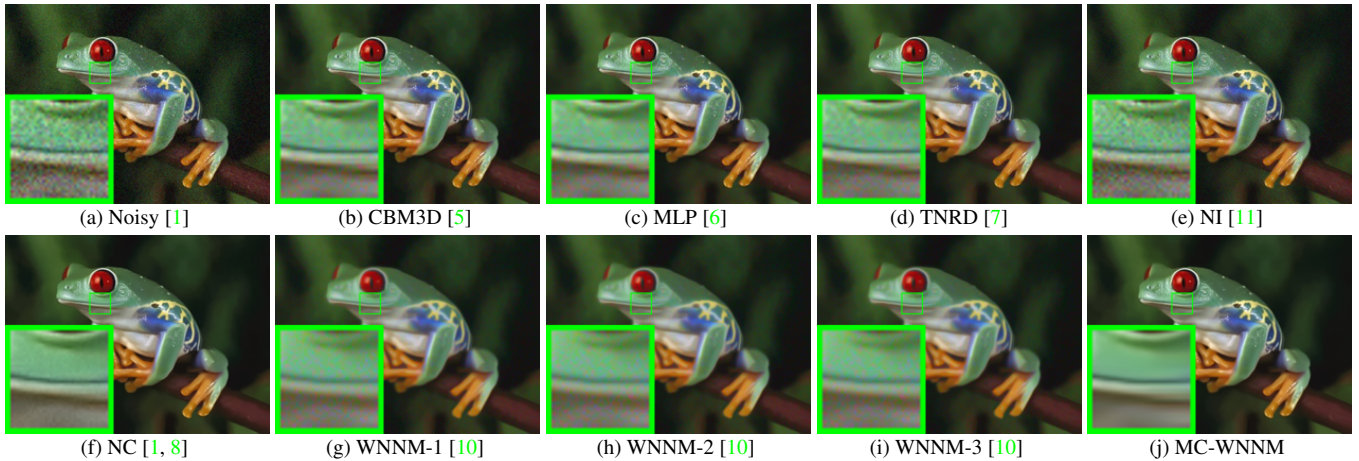


Figure 5. Denoised images of the real noisy image “Frog” [1] by different methods. The images are better to be zoomed in on screen.

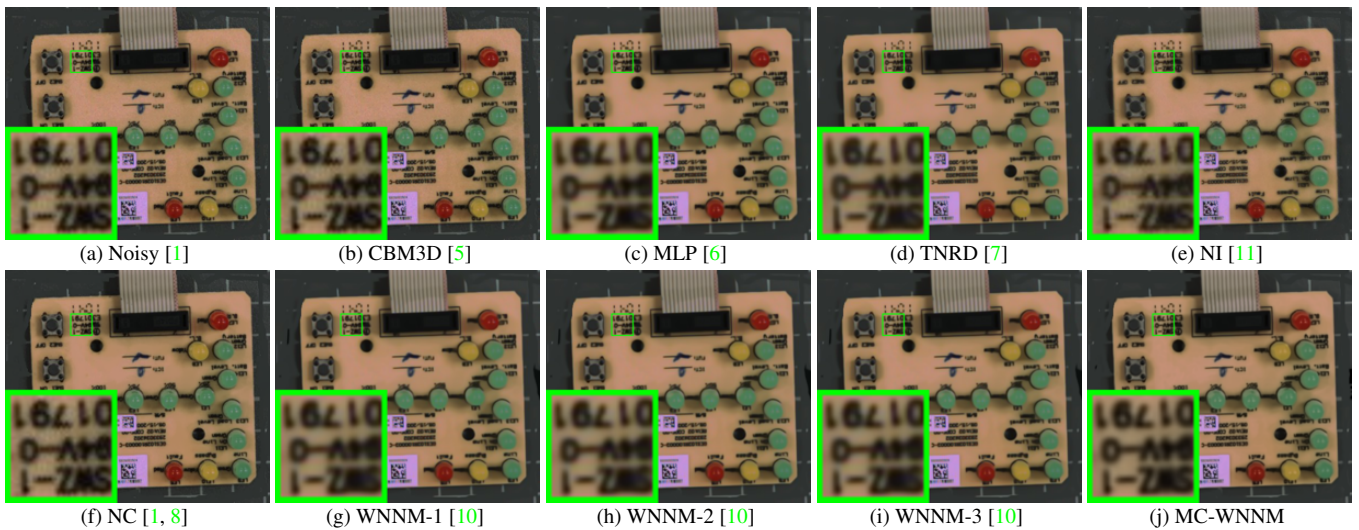


Figure 6. Denoised images of the real noisy image “Circuit” [1] by different methods. The images are better to be zoomed in on screen.

3. More visual comparisons of denoised images by different methods on the real noisy images of the dataset [1]

In this section, we give more comparisons of the state-of-the-art denoising methods on the dataset [1]. The real noisy images in dataset [1] have no “ground truth” images and hence we only compare the visual quality of the denoised images by different methods. As can be seen from Figures ??-??, our proposed method performs better than the competing methods.

4. More visual comparisons of denoised images by different methods on the real noisy images of the dataset [2]

In this section, we provide more comparisons of the proposed method with the state-of-the-art denoising methods on the 15 cropped real noisy images used in [2]. In this dataset, each scene was shot 500 times under the same camera and camera setting. The mean image of the 500 shots is roughly taken as the “ground truth”, with which the PSNR can be computed. As can be seen from Figures 13-??, in most cases, our proposed method achieves better performance than the the competing methods. This validates the effectiveness of our proposed external prior guided internal prior learning framework for real noisy image denoising.

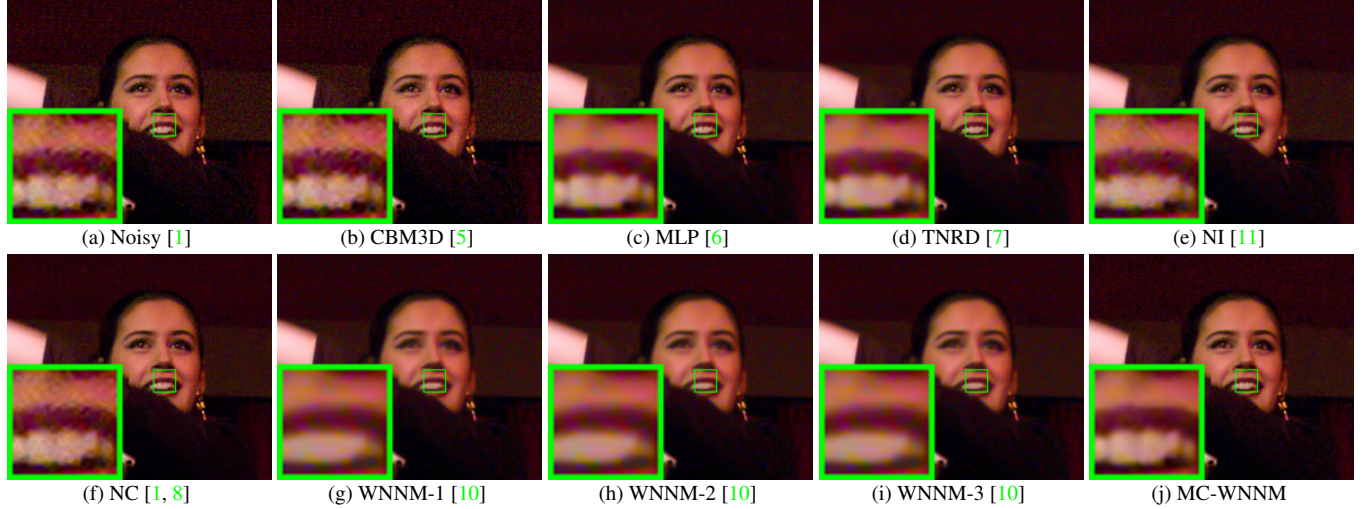
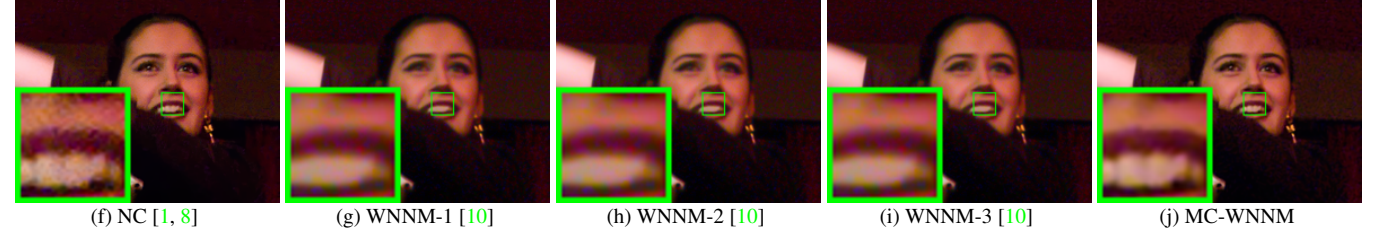
540
541
542
543
544594
595
596
597
598545
546
547
548
549599
600
601
602
603

Figure 7. Denoised images of the real noisy image “Woman” [1] by different methods. The images are better to be zoomed in on screen.

550
551
552604
605
606
607
608
609
610
611
612
613
614553
554
555
556
557
558
559
560615
616
617
618
619
620
621
622
623
624
625561
562

616

563
564
565
566
567
568
569
570
571
572

617

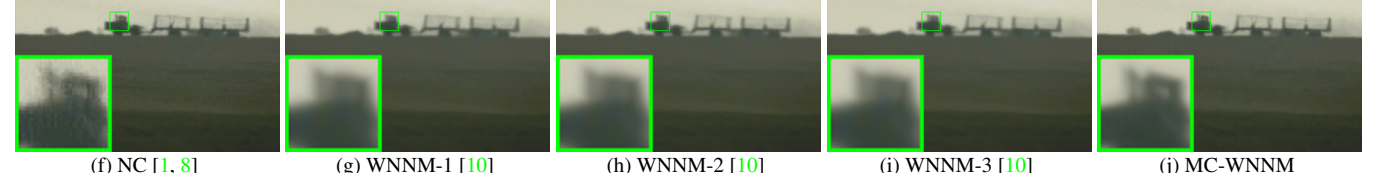
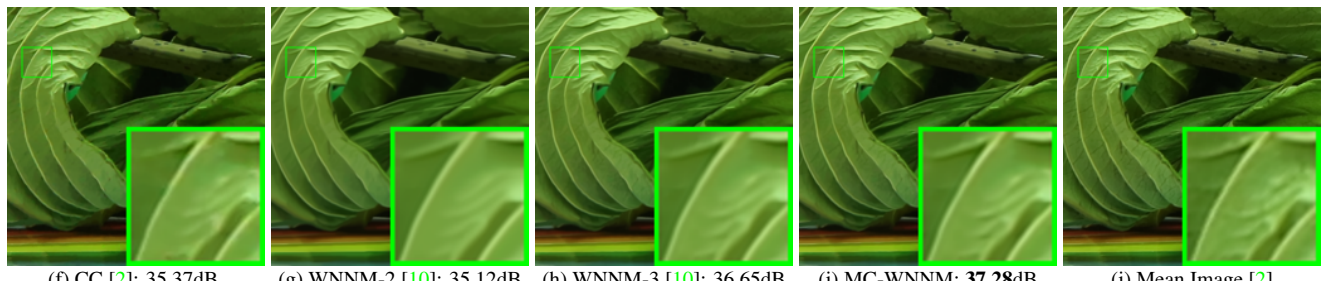
573
574
575
576
577
578
579618
619
620
621
622
623
624
625
626
627
628
629
630
631
632
633580
581
582
583
584
585
586
587634
635
636
637
638
639
640

Figure 8. Denoised images of the real noisy image “Vehicle” [1] by different methods. The images are better to be zoomed in on screen.

588
589
590
591
592
593641
642
643
644
645
646
647

648
649
650
651

(a) Noisy [2]: 33.88dB (b) CBM3D [5, 9]: 36.40dB (c) TNRD [7]: 36.47dB (d) NI [11]: 34.03dB (e) NC [1, 8]: 34.35dB

652
653
654
655
656
657
658
659

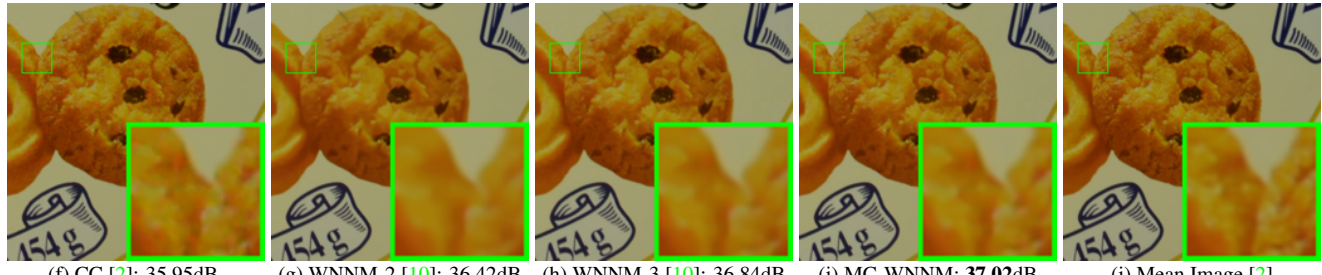
(f) CC [2]: 35.37dB (g) WNNM-2 [10]: 35.12dB (h) WNNM-3 [10]: 36.65dB (i) MC-WNNM: 37.28dB (j) Mean Image [2]

660
661
662
663
664
665
666
667
668

Figure 9. Denoised images of a region cropped from the real noisy image “Canon 5D Mark 3 ISO 3200 2” [2] by different methods. The images are better to be zoomed in on screen.

669
670
671

(a) Noisy [2]: 33.77dB (b) CBM3D [5, 9]: 35.07dB (c) TNRD [7]: 36.37dB (d) NI [11]: 35.16dB (e) NC [1, 8]: 35.34dB

672
673
674
675
676
677
678

(f) CC [2]: 35.95dB (g) WNNM-2 [10]: 36.42dB (h) WNNM-3 [10]: 36.84dB (i) MC-WNNM: 37.02dB (j) Mean Image [2]

697
698
699
700
701

Figure 10. Denoised images of a region cropped from the real noisy image “Nikon D600 ISO 3200 2” [2] by different methods. The images are better to be zoomed in on screen.

702
703
704
705
706
707
708
709
710
711
712
713
714
715
716
717
718
719
720
721
722
723
724
725
726
727
728
729
730
731
732
733
734
735
736
737
738
739
740
741
742
743
744
745
746
747
748
749
750
751
752
753
754
755

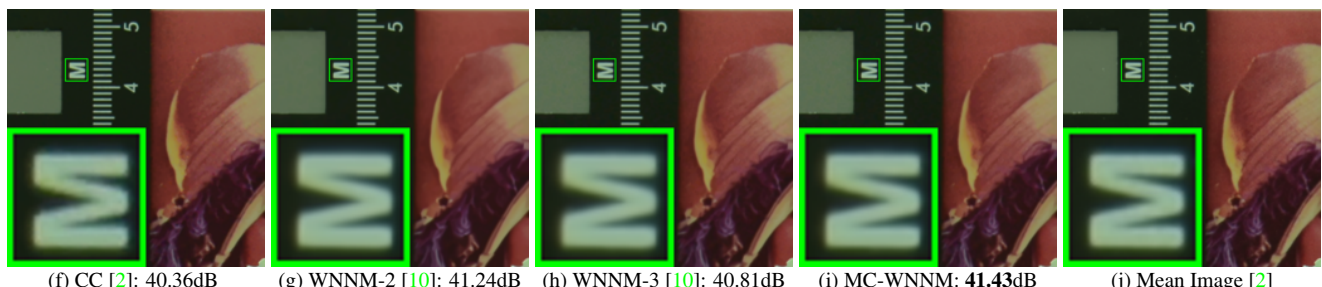
756
757
758
759810
811
812
813760
761
762
763
764
765
766
767814
815
816
817
818
819
820
821768
769
770
771
772
773
774
775
776822
823
824
825
826
827
828
829
830

Figure 11. Denoised images of a region cropped from the real noisy image “Nikon D800 ISO 1600 2” [2] by different methods. The images are better to be zoomed in on screen.

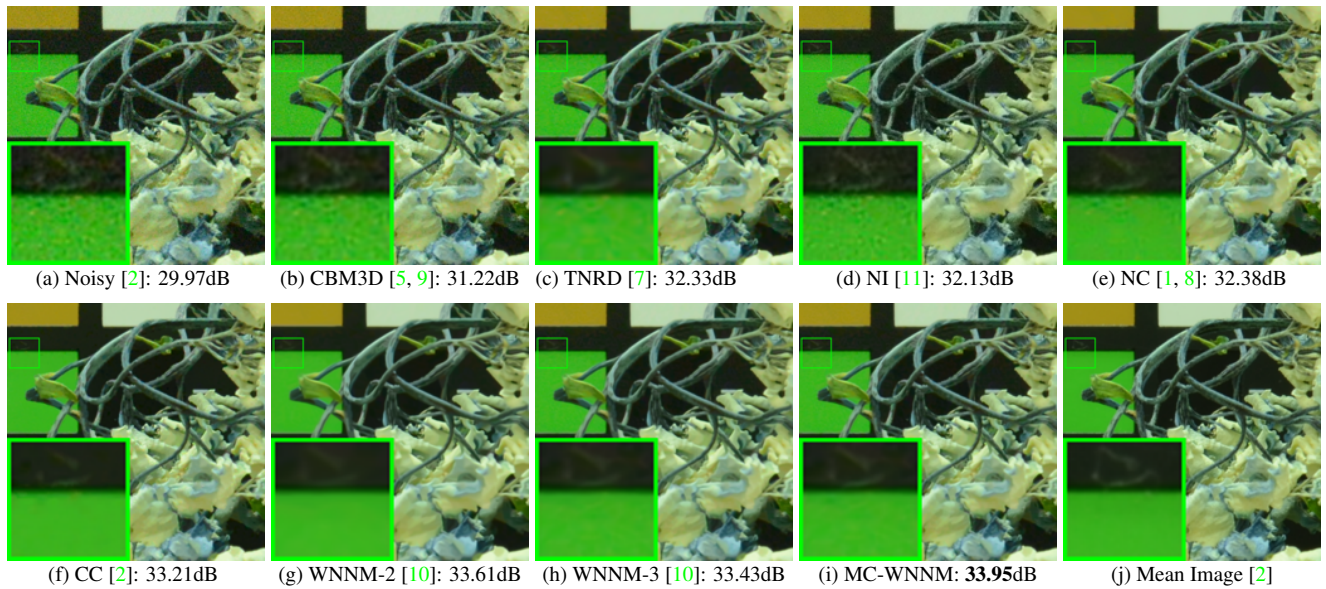
777
778
779831
832
833780
781
782
783
784
785
786834
835
836
837
838
839
840787
788
789
790
791
792
793
794841
842
843
844
845
846
847
848
849
850
851
852
853
854
855
856
857
858
859
860
861
862
863

Figure 12. Denoised images of a region cropped from the real noisy image “Nikon D800 ISO 3200 2” [2] by different methods. The images are better to be zoomed in on screen.

807

808

809

864
865
866
867
868
869
870
871
872
873
874
875
876
877
878
879
880918
919
920
921
922
923
924
925
926
927
928
929
930
931
932
933
934

900 Figure 13. Denoised images of a region cropped from the real noisy image “Nikon D800 ISO 6400 2” [2] by different methods. The images
901 are better to be zoomed in on screen.
902
903
904
905
906
907
908
909
910
911
912
913
914
915
916
917

935
936
937
938
939
940
941
942
943
944
945
946
947
948
949
950
951
952
953
954
955
956
957
958
959
960
961
962
963
964
965
966
967
968
969
970
971

References

- [1] M. Lebrun, M. Colom, and J. M. Morel. The noise clinic: a blind image denoising algorithm. <http://www.ipol.im/pub/art/2015/125/>. Accessed 01 28, 2015. 1, 3, 4, 5, 6, 7, 8, 9 1028
1029

[2] S. Nam, Y. Hwang, Y. Matsushita, and S. J. Kim. A holistic approach to cross-channel image noise modeling and its application to image denoising. *IEEE Conference on Computer Vision and Pattern Recognition (CVPR)*, pages 1683–1691, 2016. 1, 5, 7, 8, 9 1030
1031

[3] C. Eckart and G. Young. The approximation of one matrix by another of lower rank. *Psychometrika*, 1(3):211–218, 1936. 1 1032
1033

[4] S. Gu, Q. Xie, D. Meng, W. Zuo, X. Feng, and L. Zhang. Weighted nuclear norm minimization and its applications to low level vision. *International Journal of Computer Vision*, pages 1–26, 2016. 1 1034
1035

[5] K. Dabov, A. Foi, V. Katkovnik, and K. Egiazarian. Color image denoising via sparse 3D collaborative filtering with grouping constraint in luminance-chrominance space. *IEEE International Conference on Image Processing (ICIP)*, pages 313–316, 2007. 3, 4, 5, 6, 7, 8, 9 1036
1037

[6] H. C. Burger, C. J. Schuler, and S. Harmeling. Image denoising: Can plain neural networks compete with BM3D? *IEEE Conference on Computer Vision and Pattern Recognition (CVPR)*, pages 2392–2399, 2012. 3, 4, 5, 6 1040
1041

[7] Y. Chen, W. Yu, and T. Pock. On learning optimized reaction diffusion processes for effective image restoration. *IEEE Conference on Computer Vision and Pattern Recognition (CVPR)*, pages 5261–5269, 2015. 3, 4, 5, 6, 7, 8, 9 1042
1043

[8] M. Lebrun, M. Colom, and J.-M. Morel. Multiscale image blind denoising. *IEEE Transactions on Image Processing*, 24(10):3149–3161, 2015. 3, 4, 5, 6, 7, 8, 9 1045
1046

[9] K. Dabov, A. Foi, V. Katkovnik, and K. Egiazarian. Image denoising by sparse 3-D transform-domain collaborative filtering. *IEEE Transactions on Image Processing*, 16(8):2080–2095, 2007. 7, 8, 9 1047
1048

[10] S. Gu, L. Zhang, W. Zuo, and X. Feng. Weighted nuclear norm minimization with application to image denoising. *IEEE Conference on Computer Vision and Pattern Recognition (CVPR)*, pages 2862–2869, 2014. 5, 6, 7, 8, 9 1049
1050

[11] Neatlab ABSsoft. Neat Image. <https://ni.neatvideo.com/home>. 5, 6, 7, 8, 9 1053
1054

1055

1056

1057

1058

1059

1060

1061

1062

1063

1064

1065

1066

1067

1068

1069

1070

1071

1072

1073

1074

1075

1076

1077

1078

1079